Optical response of rectangular array of elliptical plasmonic particles on glass revealed by Mueller matrix ellipsometry and Finite Element modelling

Per Magnus Walmsness[1], Thomas Brakstad[1], Brage B. Svendsen[1], Jean-Philippe Banon[2,3], John C. Walmsley[4], and Morten Kildemo[1,*]

[1] *Department of Physics, NTNU Norwegian University of Science and Technology, NO-7491 Trondheim, Norway.*
[2] *Institut Langevin, ESPCI Paris, CNRS, PSL University, 1 rue Jussieu, 75005 Paris, France*
[3] *Surface du Verre et Interfaces, UMR 125 CNRS/Saint-Gobain, F-93303 Aubervilliers, France*
[4] *Department of Materials Science and Metallurgy, University of Cambridge, Pembroke Street, Cambridge CB2 3QZ, UK.*
[*] *Corresponding author: morten.kildemo@ntnu.no*

We report here on the optical response of elliptical gold particles arranged in a rectangular lattice on glass and probed at non-normal incidence in reflection using spectroscopic Mueller matrix ellipsometry in the energy range $0.73 - 5.9$ eV. The surface plasmon resonances, reshaped near the Rayleigh anomalies, are mapped out by full azimuthal rotation of the sample. The experimental Mueller matrices are discussed and interpretation is supported by finite element modelling of the Mueller-Jones matrix elements, which allows for identification of the dipolar and multipolar responses observed in the experimental spectra. The data show a strong polarization conversion around the surface plasmon resonances as a function of the azimuthal angle of incidence, also reshaped near the Rayleigh lines. An effective strong circular diattenuation is observed from the recorded Mueller matrix. We further argue the importance of Mueller matrix ellipsometry for metrology in the manufacture of metasurfaces, for understanding the effect of the lattice in metasurface design, and finally in validating computational methods.

1. INTRODUCTION

Electronics, photovoltaics or photonics manufacturing is extensively based on ellipsometry for both research and development and for on-line process control [1–3]. The traditional application of ellipsometry is in the characterization of optical properties of individual layers and stacks of layers using a multilayer formalism (in general a 4x4 matrix formalism for anisotropic layers), dispersion models or tabulated data, and effective medium models [1–3]. There is, however, a recent move towards the use of scattering Mueller matrix ellipsometry in combination with full wave modelling, in order to perform critical dimension analysis of more complex lateral structures found in electronics and photovoltaics manufacturing [3–11]. Metasurfaces are currently promising candidates for complete control of the optical wavefront using compact virtually flat optics, with applications ranging from e.g. colors, imaging (flat lenses), creation of vector beams, holography, and polarization sensitive devices [12–15].

The successful manufacture of metasurfaces beyond prototypes in the research laboratory, will similarly require a more detailed analysis and control of the optical response, ranging from individual layer thicknesses, patterning (critical dimension control), and the overall measurement of the optical response for optical devices. Furthermore, a major part of the design and calculation of the optical response of metasurfaces requires full wave computational electromagnetic modelling, typically using methods such as the Finite Element Method (FEM), Finite Difference Time Domain (FDTD) and Rigorous Coupled-Wave Analysis (RCWA). It appears thus also important to have fundamental experimental data that can be used to verify the accuracy of a given computational approach and also in order to make the link between manufacture and design. Most optical metasurfaces have for simplicity been designed for operation at normal incidence[12–15]. However, for e.g. high resolution imaging purposes of metasurfaces, one can envisage that higher angles of incidence are needed in order to preserve resolution, which

will involve complex design issues. It then becomes important to understand not only the individual particle response in terms of amplitudes and phase shifts, but also possibly the complex coupling to the lattice in terms of opening or closing of diffracted modes.

Diffractively coupled localized plasmon resonances or plasmonic surface lattice resonances (SLRs) have been extensively studied for two dimensional arrays of plasmonic nanoparticles [16–21]. They are observed as a resonant enhancement in the reflectivity (or extinction in transmission) near the Rayleigh line, where the resonance center frequency and the Q factor can be tuned by the lattice constant and the particle size [16, 17, 19]. The experimental and analytical studies have in majority considered unsupported particles (the symmetric configuration), probably since the Q-factor of the resonances can be much enhanced in this configuration [17]. However, many of the experimental studies are limited to normal incidence, while studies at oblique incidence are mostly limited to incidence along the high symmetry axis of the lattice [16–18], and to our knowledge do not consider the polarimetric properties important for metasurface applications. Thus, comparatively little work has been performed studying two dimensional arrays of supported particles on a substrate (thus including images in the so-called lattice sums appearing in the Coupled Dipole Approximation[16]), and with dimensions relevant for metasurface designs, i.e. such as recently reported using a multipole model including quadrupoles and magnetic dipoles [22]. Brakstad et al. [23] recently presented the Mueller matrix recorded in the specular direction, from reflection of a close to square lattice, consisting of truncated hemispherical particles (radius 54 nm, height 25 nm and lattice constant 210 nm) on a fused SiO_2 surface, recorded for several polar angles of incidence (45°, 55° and 65°), and for full 360 degrees azimuthal angle of incidence [23, 24]. They mapped out the resonant reshaping of the localized surface plasmon resonance (LSPR) near the Rayleigh lines, as observed in the Mueller matrix elements and the generalized ellipsometric parameters. It was shown that the spectral position of the latter plasmon resonance was slightly oscillating with azimuthal angle of incidence (dispersive), which was proposed to be a result of a weak coupling to the lattice probably of mainly dipolar origin. The sharp dip in the p-polarized reflectivity (Rayleigh-Wood anomaly) was observed in this case at a higher photon energy (well above the LSPR) at the onset of diffraction on the ambient side. It was finally reported that considerable polarization coupling was observed around the Rayleigh lines at higher photon energies, a phenomena that has been elsewise neglected in the vast literature on plasmonic 2D lattices,

In this work, through experiment and full wave simulations, we demonstrate the complex polarimetric response of a more general case: a system of truncated ellipsoidally shaped particles, arranged in a rectangular lattice, and supported by a substrate (nonsymmetric configuration). The system is shown to exhibit plasmon resonances of both dipolar and multipolar origin, in addition to strong polarization coupling and interaction of the plasmon resonances with Rayleigh anomalies. Although strictly not a localized resonance, we will for simplicity in this paper refer to the plasmon resonances as LSPRs. A major motivation was that this system can be regarded as a common prototype system for a class of reflective plasmonic metasurfaces[14], and the associated experimental data are important in order to validate computational approaches for Mueller matrix ellipsometric characterization.

2. THEORY

The change in polarization state of monochromatic light upon reflection from a smooth surface can in the non-depolarizing case be formulated by the 2×2 complex Jones matrix transforming the incoming polarization state to the reflected polarization state by the reflection amplitudes [2, 25]

$$\left(\begin{array}{c} E_p \\ E_s \end{array} \right)_r = \left(\begin{array}{cc} r_{pp} & r_{ps} \\ r_{sp} & r_{ss} \end{array} \right) \left(\begin{array}{c} E_p \\ E_s \end{array} \right)_i \quad (1)$$

In writing Eq. (1), E_p and E_s have been introduced as the plane wave electric field components that are parallel and perpendicular to the plane of incidence, respectively. The Jones matrix is extensively used in the design of metasurfaces, although mainly at normal incidence[12, 14, 15]. If the optical system is non-depolarizing, we introduce the corresponding Mueller-Jones matrix, relating the outgoing Stokes vector to the incoming Stokes vector. For such a system described by the Jones matrix $\mathbf{J}$, the corresponding Mueller-Jones matrix is given by $\mathbf{M} = \mathbf{A}(\mathbf{J} \otimes \mathbf{J}^*)\mathbf{A}^{-1}$ [26], where $\otimes$ is the Kronecker product and the square matrix $\mathbf{A}$ is given in the literature [26]. The Mueller Jones elements are also listed elsewhere [23, 26, 27], but repeated here for completeness:

$$M_{11} = \frac{1}{2} \left(|r_{pp}|^2 + |r_{sp}|^2 + |r_{ps}|^2 + |r_{ss}|^2 \right)$$
$$M_{12} = \frac{1}{2} \left(|r_{pp}|^2 + |r_{sp}|^2 - |r_{ps}|^2 - |r_{ss}|^2 \right)$$
$$M_{13} = \mathrm{Re} \left(r_{pp} r_{ps}^* + r_{sp} r_{ss}^* \right)$$
$$M_{14} = \mathrm{Im} \left(r_{pp} r_{ps}^* + r_{sp} r_{ss}^* \right)$$
$$M_{21} = \frac{1}{2} \left(|r_{pp}|^2 - |r_{sp}|^2 + |r_{ps}|^2 - |r_{ss}|^2 \right)$$
$$M_{22} = \frac{1}{2} \left(|r_{pp}|^2 - |r_{sp}|^2 - |r_{ps}|^2 + |r_{ss}|^2 \right)$$
$$M_{23} = \mathrm{Re} \left(r_{pp} r_{ps}^* - r_{sp} r_{ss}^* \right)$$
$$M_{24} = \mathrm{Im} \left(r_{pp} r_{ps}^* - r_{sp} r_{ss}^* \right) \quad (2)$$
$$M_{31} = \mathrm{Re} \left(r_{pp} r_{sp}^* + r_{ps} r_{ss}^* \right)$$
$$M_{32} = \mathrm{Re} \left(r_{pp} r_{sp}^* - r_{ps} r_{ss}^* \right)$$
$$M_{33} = \mathrm{Re} \left(r_{pp} r_{ss}^* + r_{ps} r_{sp}^* \right)$$
$$M_{34} = \mathrm{Im} \left(r_{pp} r_{ss}^* - r_{ps} r_{sp}^* \right)$$
$$M_{41} = -\mathrm{Im} \left(r_{pp} r_{sp}^* + r_{ps} r_{ss}^* \right)$$
$$M_{42} = -\mathrm{Im} \left(r_{pp} r_{sp}^* - r_{ps} r_{ss}^* \right)$$
$$M_{43} = -\mathrm{Im} \left(r_{pp} r_{ss}^* + r_{ps} r_{sp}^* \right)$$
$$M_{44} = \mathrm{Re} \left(r_{pp} r_{ss}^* - r_{ps} r_{sp}^* \right)$$

The off-block-diagonal elements of $\mathbf{M}$ represent *polarization coupling*. The Mueller matrix is conventionally normalized by the M_{11} element. Here the normalized Mueller matrix is denoted by $\mathbf{m} = [m_{ij}]$ with $m_{ij} = M_{ij}/M_{11}$, $(i, j = 1, \dots, 4)$ so that trivially $m_{11} \equiv 1$. Hence, no reference measurement is required beyond standard calibration.

For a 2D periodic system with lattice parameters a_1 and a_2 (see Fig. 1), the fields in regions of space with constant (with

respect to the spatial variable) dielectric function $\epsilon(\omega, \mathbf{x})$ are plane waves with in-plane (here denoted by a parallel symbol) wave vectors which only differ by a reciprocal lattice vector $\mathbf{G}_{mn} = m \frac{2\pi}{a_1}\hat{\mathbf{x}}_1 + n \frac{2\pi}{a_2}\hat{\mathbf{x}}_2$, where (m,n) are integers. When a wave with wave vector $\mathbf{k} = \mathbf{k}_3 + \mathbf{k}_\parallel$ is incident on the system, the wave vectors $\mathbf{q} = \mathbf{q}_3 + \mathbf{q}_\parallel$ of the scattered waves must satisfy the dispersion relation $\epsilon(\omega)\frac{\omega^2}{c^2} - \mathbf{q}^2 = 0$ and conservation of in-plane momentum $\mathbf{q}_\parallel = \mathbf{k}_\parallel + \mathbf{G}_{mn}$. Rayleigh anomalies are defined by the opening or closing of propagating (diffracting) waves, i.e. when a wave transitions from being evanescent to propagating (or vice versa). The condition for a Rayleigh line is found by setting $|\mathbf{q}_3| = 0$, leading to

$$\left(\frac{m\lambda_0}{a_1} + \cos\phi_0\sin\theta_0\right)^2 + \left(\frac{n\lambda_0}{a_2} + \sin\phi_0\sin\theta_0\right)^2 = N^2 \quad \textbf{(3)}$$

Here λ_0 is the wavelength of the incident wave (coming from air), N is the refractive index of the medium (here air or SiO$_2$) and the angles are such that $\mathbf{k} = \frac{2\pi}{\lambda_0}(\sin\theta_0\cos\phi_0, \sin\theta_0\sin\phi_0, -\cos\theta_0)$ (see Fig. 1). The form in Eq. (3) is useful, as it allows to either solve for the Rayleigh lines, the lattice constants or the refractive index of the substrate.

The simulated Jones matrix elements of the system, and thus the corresponding Mueller-Jones elements, were extracted from the S-parameters calculated using COMSOL multiphysics 5.2, with the wave optics module, through two separate calculations for p (TM) and s (TE) polarized incidence. The unit cell used periodic boundary conditions and all diffracted modes where included in the calculations. The frequency dependent dielectric function for the Au particles and SiO$_2$ substrate was taken from ellipsometric analysis of the deposited Au film and data from the Woolam software database, respectively. The lattice parameters and particle radii used in the simulations were extracted from a fitting routine using the reduced Rayleigh equations [11]. The calculations where performed in the energy range $\hbar\omega = 0.73 - 4.96$ eV ($1700 - 250$ nm), in steps of 5 nm, at polar angle of incidence $\theta_0 = 55°$, where each frequency was swept for azimuthal angles of incidence $\phi_0 = 0° - 180°$ in steps of 5°. The resistive power heat loss function defined as $L = \int_V \mathbf{J} \cdot \mathbf{E}\,dV$, where V is the domain volume of the Au particle, $\mathbf{E}(\mathbf{x})$ is the electric field (frequency domain) and $\mathbf{J}(\mathbf{x})$ is the current density, was calculated for both input polarisations. The simulation time for p-polarized incidence (including all azimuthal angles of incidence), was 2 minutes for $\hbar\omega = 0.73$ eV and 2 hours and 27 minutes for $\hbar\omega = 4.96$ eV on a computer equipped with an Intel i7-3930K processor and 32 GB of RAM, running under windows 7. The equivalent times for s-polarization were 2 minutes ($\hbar\omega = 0.73$) and 2 hours and 18 minutes ($\hbar\omega = 4.96$).

3. EXPERIMENTAL

We study a two-dimensional photonic crystal made from a rectangular array of hemi-ellipsoidal gold (Au) particles supported by a fused silica SiO$_2$ substrate. The sample was produced by first evaporating a thin film of Au onto a clean (and flat) UV-grade fused silica surface using an ebeam evaporator (Pfeiffer Vacuum Classic 500). The deposited film thickness was 40 nm, and the film was smooth but polycrystalline. The Au nanostructures were then produced by Focused Ion Beam (FIB)-milling using Ga ions (FEI Helios Dual-beam FIB). The sample was designed and manufactured to make up approximately truncated (half) Au ellipsoids supported directly by the glass substrate without an adhesion layer. Fig. 1 shows a SEM image of the
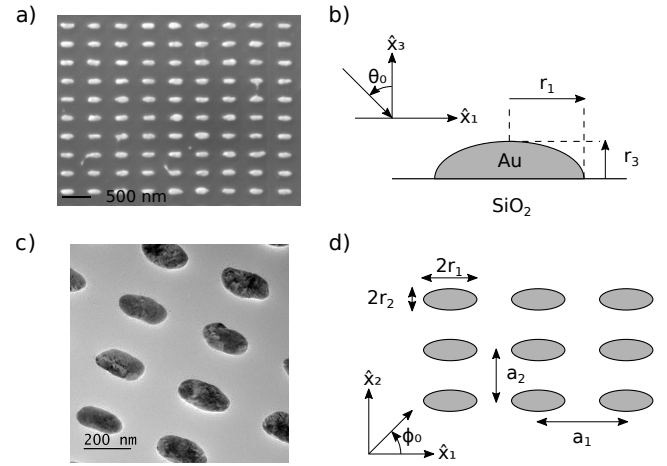

Fig. 1. a) Scanning Electron Microscopy image of the sample. b) Schematic of the geometry of the particles used in the FEM modelling. c) Transmission Electron Microscopy image of similar sample produced on a Si$_3$N$_4$ membrane (note that this sample has different dimensions, but was otherwise produced under identical conditions using FIB milling). d) Schematic of the lattice and particle geometry (top view).

sample (as well as a transmission electron microscopy (TEM) image of a sample similar to the one studied here), and schematics of the particle and lattice geometry used in the modelling. From SEM characterization of the sample, the particle height $r_3 = 40 \pm 10$ nm, the lattice parameters $a_1 = 473 \pm 10$ nm and $a_2 = 322 \pm 7$ nm, and the particles in-plane radii $r_1 = 107 \pm 4$ nm and $r_2 = 47 \pm 4$ nm could be estimated. The optical response of the sample was investigated by azimuthal angle-resolved spectroscopic Mueller matrix ellipsometry in the reflected specular direction. A variable angle multichannel dual rotating compensator Mueller matrix ellipsometer (RC2) from JA Woollam Company was used.

Our instrument has a 150W Xe source and operates in the spectral range from 210 nm (5.9 eV) to 1700 nm (0.73 eV). The total area milled with the FIB was limited to $240\,\mu m \times 240\,\mu m$ and therefore UV transparent achromatic focusing and collection lenses with a focal length of 20 mm and a numerical aperture of approximately 0.15 were used [23]. The spatial coherence of the system is an important parameter in terms of estimating depolarization properties [28] of metasurfaces or 2 dimensional plasmonic lattices. Furthermore, to resolve nominally sharp features in spectra (such as e.g. coupled plasmon surface lattice resonances) a reasonable coherence length is required (typically an illumination numerical aperture of NA<0.1 is reported [16]). The pin-hole on the source side was selected to its maximum diameter of D_s=100 µm in order to maximize the signal. This pin-hole is here regarded as the incoherent source area for the estimation of the spatial coherence. The spatial (or transverse) coherence length for the paraxial ray-bundle is then estimated to $200\lambda_0$ (which will be the spatial coherence length for the collimated beam). However, including the full numerical aperture of the focusing lens, the coherence length strongly reduces to approximately $\lambda_0/0.15$. The spot diameter was estimated to be approximately 100 µm at normal incidence. No major depolarization was observed from the measured Mueller matrix of the sample as long as the beam stayed inside the milled area. In the current data set, the Mueller matrices in the range $\phi_0 = 0° - 90°$
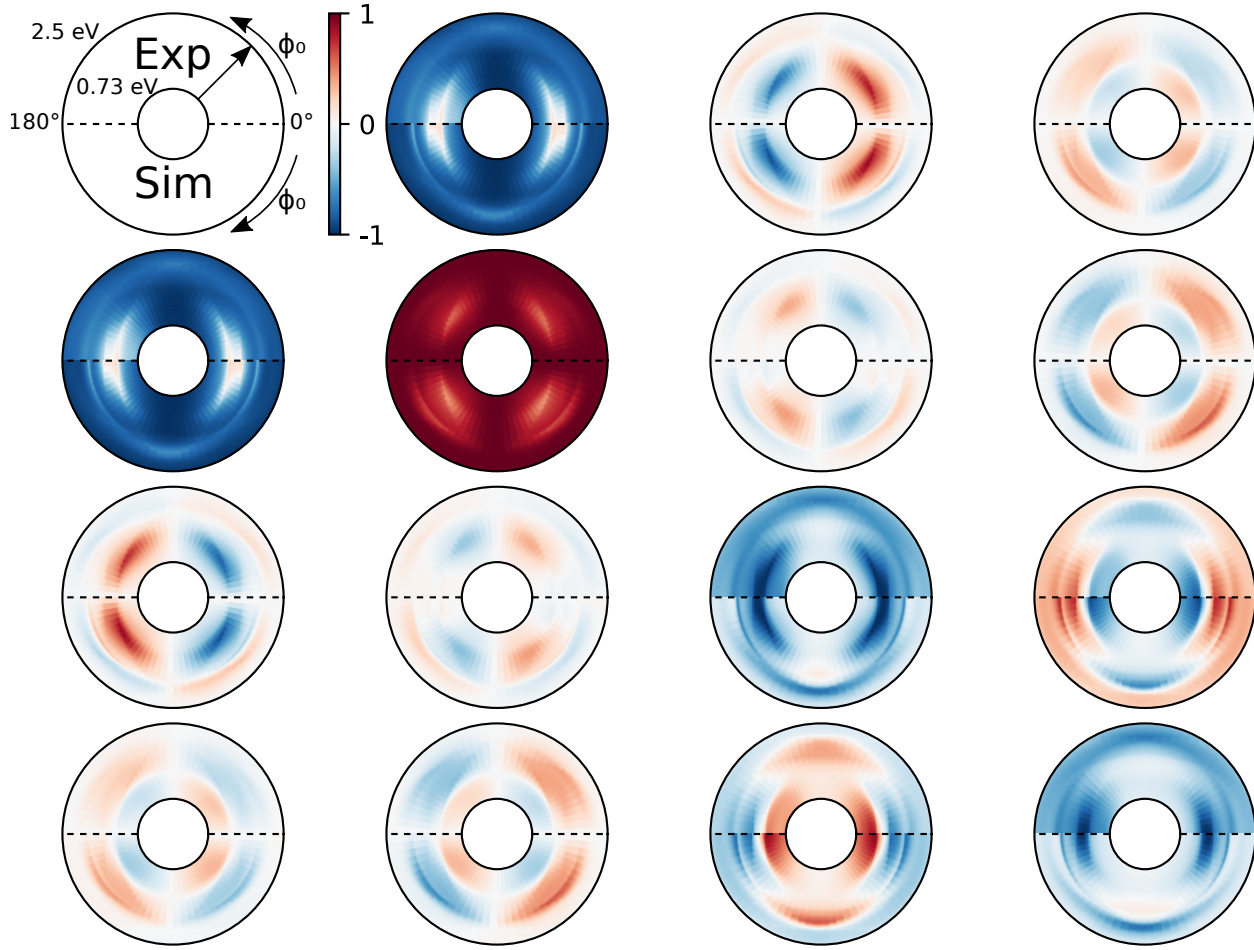
Fig. 2. Normalized Mueller matrix elements $m_{ij} = M_{ij}/M_{11}$ ($i,j = 1, \ldots, 4$) color coded and shown as functions of the photon energy $\hbar\omega$ (radial variable) in the range $0.73 - 2.5$ eV and the azimuthal angle of incidence (angular variable) $\phi_0 \in [0°, 180°]$. The polar angle is $\theta_0 = 55°$. The upper halves of the polar plots are experimental m_{ij}-elements, and the corresponding lower halves are simulation results obtained from the FEM model using parameters given in the text. Notice from the schematic in the upper-left corner the positive direction assumed for the azimuthal angle of incidence ϕ_0, comparison between measured and simulated results should be made symmetrically with respect to the horizontal black dashed lines of each element.

have depolarization less than 0.5 %. A larger depolarization of 2 % was observed in the range $\phi_0 = 90° - 180°$ where the beam is believed to have partially touched the boundaries of the milled area (consisting of the unmilled Au film).

4. RESULTS AND DISCUSSION

A. Overview of the experimental and simulated Mueller matrix

The experimental results obtained as functions of the azimuthal angle of incidence $\phi_0 \in [0°, 180°]$ and photon energy $\hbar\omega$ for the polar angle of incidence $\theta_0 = 55°$ are shown in the upper halves of the contour plots of the normalized Mueller matrix in Fig. 2. Here the energy increases in the radial direction from $\hbar\omega = 0.73$ eV (inner circle) to $\hbar\omega = 2.5$ eV (outer circle). Note that the full $0° - 360°$ data set (not presented here) shows the expected inversion symmetry, except for small deviations caused by the beam partially touching the boundaries, which here happened for certain azimuthal angles of incidence. The Mueller matrix elements show in general strong azimuthal dependent features related to localized surface plasmon resonances (LSPRs). For a particle that is rotationally symmetric around the x_3 direction,

we previously showed that the LSPR related feature in the m_{12} element would trace out nearly a circle, only weakly affected by the lattice [23]. In the current case, this LSPR feature is split in two; a low energy part and a high energy part, due to the asymmetry of the particles. Another prominent optical feature of the system is the significant polarization coupling observed around the LSPRs. This can be seen in the off-diagonal blocks of the Mueller matrix, which are nominally zero when there is no polarization coupling, i.e. $r_{ps} = r_{sp} = 0$ in Eq. (2). Finally, it is possible to observe from Fig. 2 that the LSPR related features are reshaped near boundaries in $(\hbar\omega, \phi_0)$ parameter space. These boundaries are near the Rayleigh lines/anomalies, as discussed below.

The simulated normalized Mueller matrix elements using FEM (COMSOL) in the energy range $\hbar\omega = 0.73 - 2.5$ eV are shown in the lower half of Fig. 2. The particle radii used in the simulation were $r_1 = 113.2$ nm, $r_2 = 47.4$ nm and $r_3 = 34.4$ nm, and the lattice parameters were $a_1 = 443.9$ nm and $a_2 = 315.4$ nm. It is observed that the main spectral features agree well with the experimental counterparts. In particular, the azimuthal angle-dependent LSPR features, which we mainly attribute to
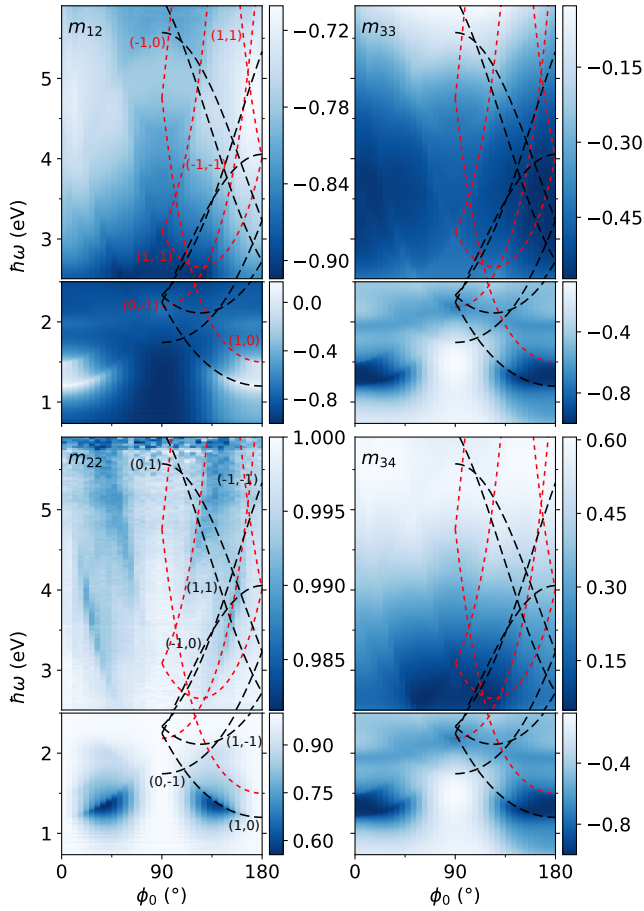
Fig. 3. Measured block diagonal Mueller elements as a function of photon energy $\hbar\omega$ and azimuthal angle of incidence ϕ_0 for polar angle $\theta_0 = 55°$. The data is color coded and shown in two energy ranges separated at 2.5 eV. The dashed red lines correspond to the lowest order Rayleigh lines for air (labelled with red text in the m_{12} element) and the dashed black lines correspond to the lowest order Rayleigh lines for SiO$_2$ (labelled with black text in the m_{22} element). The lines are symmetric about $\phi_0 = 90°$.

Fig. 4. Measured upper off-block diagonal Mueller elements as a function of photon energy $\hbar\omega$ and azimuthal angle of incidence ϕ_0 for polar angle $\theta_0 = 55°$. The data is color coded and shown in two energy ranges separated at 2.5 eV. The dashed red lines correspond to the lowest order Rayleigh lines for air (labelled with red text in the m_{13} element) and the dashed black lines correspond to the lowest order Rayleigh lines for SiO$_2$ (labelled with black text in the m_{23} element). The lines are symmetric about $\phi_0 = 90°$.

dipolar resonances for the E-field vector along the principal axes of the hemi-ellipsoids, seem well reproduced by the simulation. The position of the LSPRs are slightly offset with respect to the experimental data in the energy range shown, and larger discrepancies are found at higher energies (not shown here). This is believed to be due to uncertainties in the lattice parameters and particle geometry. In addition, it was found that an over milling into the substrate had occurred when the particles were manufactured, resulting in a dielectric mound beneath the particles. This mound (and any possible inclusion of Ga ions), was for simplicity not included in the model. For a similar system based on isotropic particles, it has been demonstrated that the reduced Rayleigh equations could be integrated into an optimization scheme, and allowed for fast determination of all relevant morphological parameters, including the mound height [11]. However, having established that a FEM model reproduce the experimental data with sufficient accuracy and that the experimental data contains limited depolarization allows for analyzing and interpreting the recorded optical spectra through the calculation of quantities not accessible in common optical
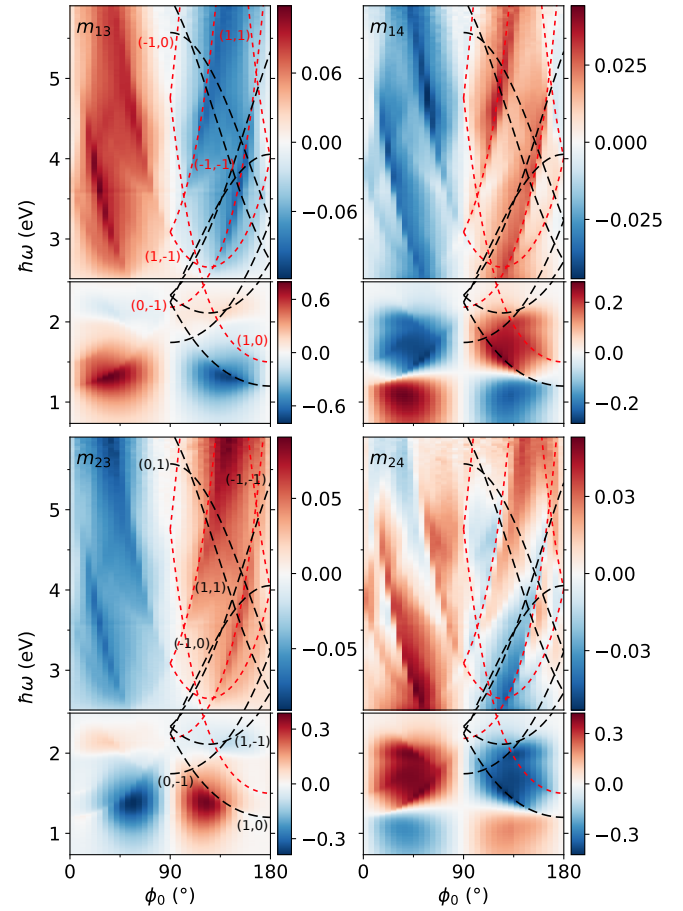
techniques, such as e.g. the complex Jones elements. These elements are also fundamental in the design of metasurfaces, which is often guided by the specular Jones Matrix and concepts from diffraction theory.

B. Symmetries of the Mueller matrix
For each azimuthal angle of incidence, the symmetries in the Mueller matrix in Fig. 2 correspond to a general biaxial system [29]. For such a system, the following set of relations are valid: $m_{12} - m_{21} = 0$, $m_{13} + m_{31} = 0$, $m_{14} - m_{41} = 0$, $m_{23} + m_{32} = 0$, $m_{24} - m_{42} = 0$ and $m_{34} + m_{43} = 0$, which is equivalent to setting $r_{\mathrm{ps}} = -r_{\mathrm{sp}}$ in Eq. (2). These sums are trivially 0 in the modelled Mueller Jones elements, and within ± 0.075 in the experimental data.

Due to the common symmetries of the Mueller matrix, we now focus on the main block diagonal elements (m_{12}, m_{22}, m_{33} and m_{34}) in Fig. 3, and the upper off-block diagonal elements (m_{13}, m_{14}, m_{23} and m_{24}) in Fig. 4, as a function of the azimuthal angle of incidence and photon energy. All figures are maps where the color indicates the value of the measured Mueller
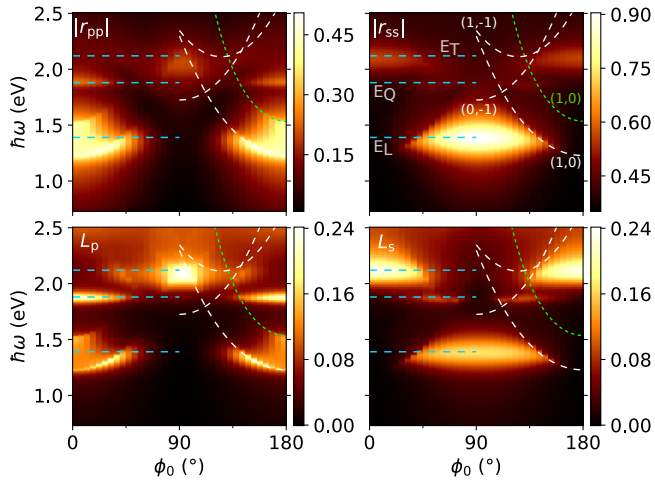
Fig. 5. The top figures are simulated reflection amplitudes $|r_{pp}|$ (top left figure) and $|r_{ss}|$ (top right figure) using the FEM model. The bottom figures show the corresponding power dissipation in the particles, for incident p-polarization (L_p bottom left figure), and s-polarization (L_s bottom right figure). The lowest order Rayleigh lines for air (green) and SiO$_2$ (white) are superposed on the data. Horizontal blue lines mark the position of the $E_L = 1.39$ eV, $E_Q = 1.88$ eV and $E_T = 2.12$ eV resonances. The polar angle is $\theta_0 = 55°$.

Fig. 6. The simulated reflection amplitudes $|r_{ss}|$ and $|r_{pp}|$ at $\phi_0 = 0°$ and $\phi_0 = 90°$, and $|r_{ps}|$ at $\phi_0 = 45°$, highlighting the three plasmon resonances $E_L = 1.39$ eV, $E_Q = 1.88$ eV and $E_T = 2.12$ eV, fully mapped out in Fig. 5. The dashed vertical lines correspond to the $(-1,0)$ Rayleigh lines in air and in glass at $\phi_0 = 0°$. The polar angle is $\theta_0 = 55°$.

matrix element. Each element is presented in two subfigures, one for lower photon energies $\hbar\omega < 2.5$ eV (as presented in Fig. 2) and one for higher photon energies $\hbar\omega > 2.5$ eV. The lowest order Rayleigh lines for air (red) and SiO$_2$ (black) are also shown. Note that, for increased visibility of the data, the lines are only shown for $\phi_0 = 90° - 180°$ as they are symmetric about $\phi_0 = 90°$. The symmetry of the Mueller elements (with respect to the azimuthal angle ϕ_0) follows the symmetry of the sample, except for small deviations close to $\phi_0 = 180°$, most visible in the m_{12}, m_{33} and m_{34} elements in Fig. 3. We attribute these deviations to the increased depolarization (due to beam wander) at these angles of incidence, as discussed in the experimental section. All elements show features related to LSPRs for the lower photon energies.

C. Identification of LSPRs and interaction with Rayleigh anomalies

The Mueller elements can be interpreted directly, but the interpretation becomes more convenient when also inspecting the amplitudes of the simulated Jones elements $|r_{pp}| = \sqrt{R_{PP}}$ and $|r_{ss}| = \sqrt{R_{SS}}$ together with the power loss in the Au particles L_p and L_s for incident p- and s-polarized light, respectively. The reflectivities R_{PP} and R_{SS} were not measured in this work, but they can be extracted with some loss of accuracy from the measured Mueller matrix, if a proper reference measurement is additionally performed. The reflection amplitudes and power losses for s- and p-polarized light are fully mapped out as functions of energy ($\hbar\omega \in [0.73, 2.5]$ eV) and azimuthal angle of incidence ($\phi_0 \in [0°, 180°]$) in Fig. 5. The reflection amplitudes along high symmetry directions are further shown in figure Fig. 6. Through Figs. 3, 4, 5 and 6 we identify three main LSPRs, and interpret them as resonances corresponding to cases i) - iii):

i) The electric field is along the long axis of the particle (i.e. along $\hat{x}_1$ in Fig. 1) with corresponding resonance $E_L = 1.39$ eV.
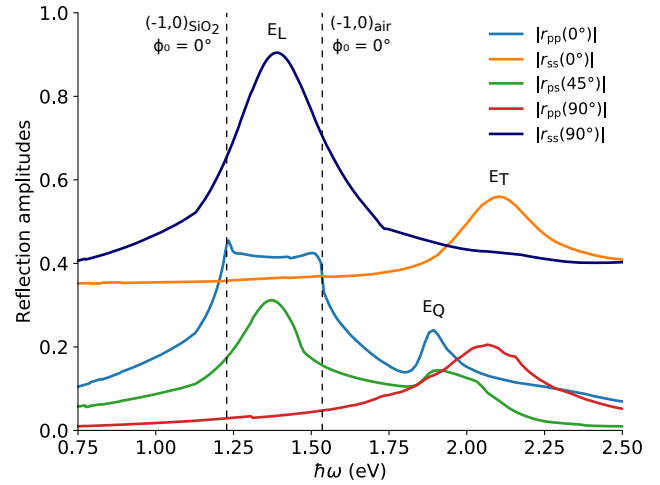
This resonance is readily observed in the experimental data in the upper block Mueller elements in Fig. 3. It is also observed in the simulated $|r_{pp}|$ at $\phi_0 = 0°$ and $|r_{ss}|$ at $\phi_0 = 90°$, as seen in Fig. 5 (the position of the resonance is indicated by a dotted blue line) and in Fig. 6. The simulated resistive loss with s-polarized incidence (bottom right in Fig. 5) also clearly shows the E_L resonance for $\phi_0 = 90°$, while p-polarized incidence gives as expected a strong loss feature around E_L for $\phi_0 = 0°$ and 180°. The shape of the resonance is very different under p- and s-polarized incidence. In $|r_{ss}|$ and L_s the resonance is broad (due to the imaginary part of the dielectric function of Au), while for p-polarized incidence the resonance shows two prominent spectral features. The latter two features are a result of the Rayleigh lines $(\pm1,0)_{SiO_2}$ and $(\pm1,0)_{air}$ overlapping the normally broad non-dispersive LSPR and consequently reshaping it, as seen in Figs. 5 and 6. Indeed, the amplitude $|r_{pp}|$ in Figs. 5 and 6 shows that the reflection increases when approaching the resonance, but drops in two stages; first when the photon energy is increased beyond the opening of the $(\pm1,0)_{SiO_2}$ transmissive mode and second when crossing the $(\pm1,0)_{air}$ reflective mode. This is also seen in L_p in Fig. 5 where the absorption loss is reduced when the photon energy is increased and the Rayleigh lines are crossed. It is further observed that for s-polarized light the resonance appears bounded by the Rayleigh lines, suggesting an abrupt redistribution of energy when the first transmissive diffractive channels are opened. The apparent sharp features/peaks around the Rayleigh lines, particularly for $|r_{pp}|$ at $\phi_0 = 0°$, could be interpreted as diffractively coupled plasmon surface lattice resonances[16–18, 22] with low Q factors. However, the current system appears better described by redistribution of energy upon opening of diffracted channels.

ii) The much weaker LSPR feature located at $E_T = 2.12$ eV (indicated by blue dotted horizontal line in Fig. 5), where the E-field is along the short axis of the particle (i.e. along $\hat{x}_2$ in Fig. 1). This resonance is seen as weak features in $|r_{ss}|$ at $\phi_0 = 0°$ and in $|r_{pp}|$ at $\phi_0 = 90°$, see Figs. 5 and 6. It is, however, highly visible in the loss L_s under s-polarized incidence at $\phi_0 = 0°$, and
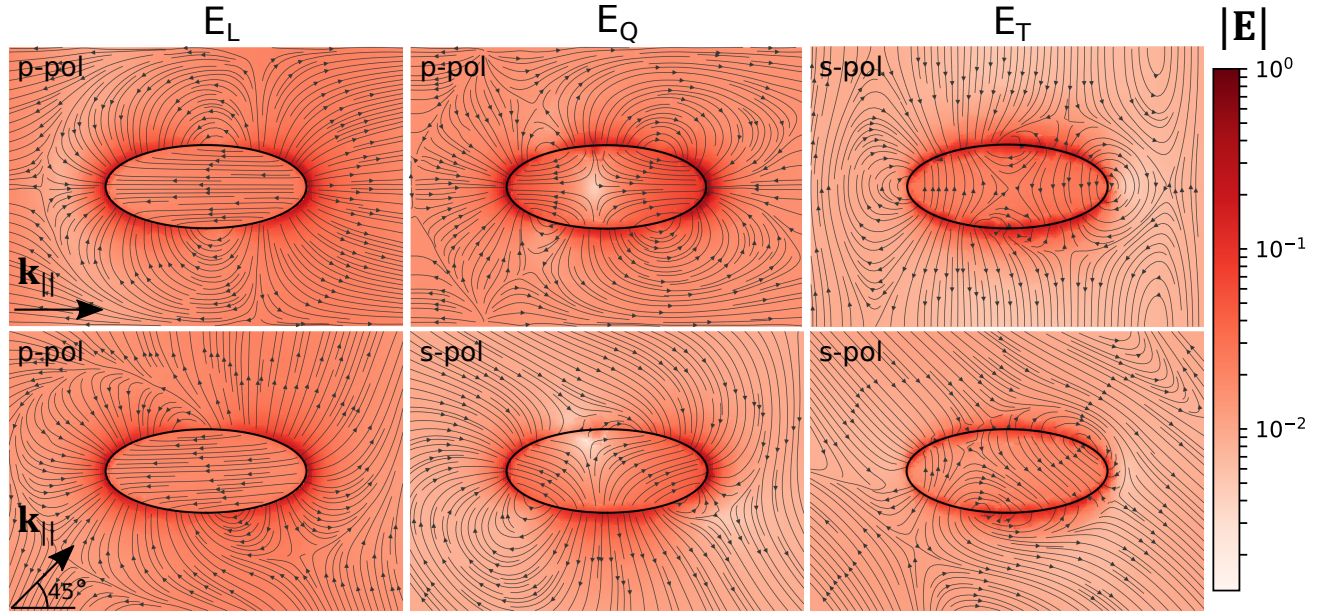
Fig. 7. The electric field norm and in-plane electric field directions in the x_1x_2-plane at the main LSPRs for a set of azimuthal angles of incidence and polarizations at polar angle $\theta_0 = 55°$, simulated with the FEM model. The electric field norm is color coded on a log-scale and the direction of the in-plane electric field is visualized by streamlines. The upper row correspond to azimuthal angle of incidence $\phi_0 = 0°$, and the lower row to $\phi_0 = 45°$. The columns correspond to the three LSPRs $E_L = 1.39$ eV, $E_Q = 1.88$ eV and $E_T = 2.12$ eV.

in the loss L_p under p-polarized incidence at $\phi_0 = 90°$, shown in Fig. 5. The LSPR features for both s- and p-polarization, appear here bounded by the Rayleigh lines.

iii) An additional loss feature is observed at $E_Q = 1.88$ eV, indicated by the dotted blue horizontal line in Fig. 5). This resonance is strongly excited under p-polarized incident light, as seen from L_p (bottom left Fig. 5) and $|r_{pp}|$ in Figs. 5 and 6, suggesting initially that it may be a dipolar resonance in the r_3 dimension of the particles. However, such a resonance would nominally for a smaller particle (in the quasistatic approximation) be expected rather near the E_T resonance [24]. It is possible to observe the resonance as a weak feature in the m_{12} element, and more indirectly in the m_{33} and m_{34} elements of the experimental data in Fig. 3. It is highly interesting to note that the resonance is not excited by s-polarized incidence at $\phi_0 = 90°$ or $\phi_0 = 0°$, but appear in the range $\phi_0 \approx 20° - 75°$, as seen from L_s and $|r_{ss}|$ in Fig. 5. This contradict the notion that E_Q is an out of plane resonance, as this resonance should not be excited by s-polarized light. It therefore appears more likely that the E_Q resonance is of a multipolar origin. However, multipolar features of freestanding particles nominally appear for more elongated particles (higher aspect ratios)[30], but here the presence of the substrate probably modifies the conditions and hence may allow for a multipole.

D. Polarization conversion

Finally, a strong polarization conversion related to the plasmon resonances are observed from the off-block diagonal elements in Figs. 2 and 4, and in the m_{22} element in Fig. 3. It is understood from Eq. (2) that these selected elements convey better the polarization conversion (through r_{sp} and r_{ps}) although also present in the remaining block diagonal Mueller matrix elements. The simulated cross polarization reflection amplitude $|r_{ps}| = |r_{sp}|$ is shown in Fig. 6 for azimuthal incidence of $\phi_0 = 45°$, showing

strong polarization conversion around the E_L and E_Q resonances, and weaker conversion around the E_T resonance. The Rayleigh lines are similarly observed to shape the polarization coupling near the plasmon resonances, but also far from any resonances. This is evident in the off-block diagonal elements for higher energies shown in Fig. 4. The magnitude of the polarization coupling in this energy region is comparatively small, but the relative changes in the spectra seem correlated to the Rayleigh anomalies, although it must be noted that not all of the anomalies are directly visible in the data. With a more well defined incident **k** vector, these anomalies may be resolvable. However, it is possible that the energy carried by these modes is small, resulting in changes in the specular beam below the noise floor of the normalized Mueller elements, i.e. the limit at which the ellipsometer can measure when using focusing and collection optics ($\approx 10^{-4}$).

E. Analysis and visualization of resonances using FEM data

In order to better understand the features of the LSPRs the norm of the electric field and the direction of the in-plane component of the electric field vector are visualized in Fig. 7 in the x_1x_2-plane (i.e. $x_3 = 0$), under p- and s- polarized incidence. The top left panel in Fig. 7 shows the E_L resonance observed for p-polarized light at $\phi_0 = 0°$. It is clearly a strong dipole resonance. For diffractively coupled plasmon surface lattice resonances with high Q factor, a highly visible lattice mode could be observed from inspection of the the electric field in energy regions close to Rayleigh anomalies [16–18]. In the current system, we do not observe such modes close to the two Rayleigh anomalies $(-1,0)_{SiO_2}$ and $(-1,0)_{air}$.

The top middle panel in Fig. 7 shows the E_Q resonance observed for incident p-polarized light at $\phi_0 = 0°$. Interestingly, this resonance is observed to have the characteristics of a quadrupole resonance. The authors are unaware of previ-
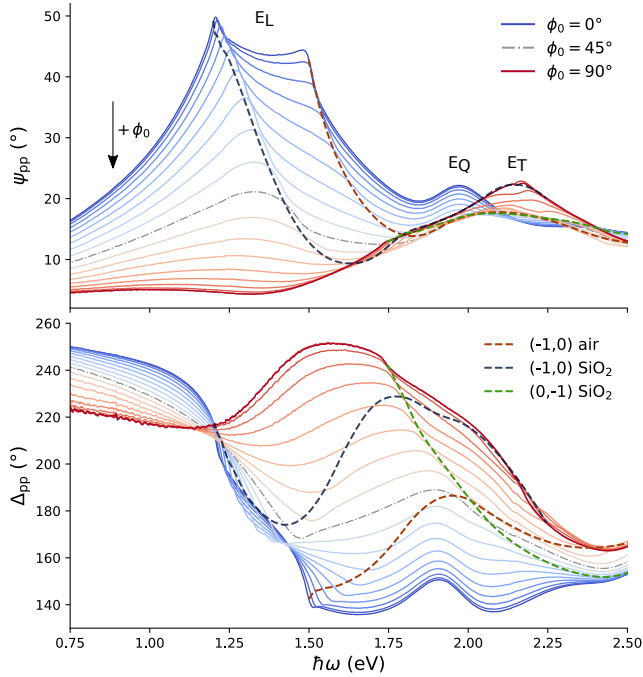
Fig. 8. The experimental generalized ellipsometric parameters ψ_{pp} (top figure) and Δ_{pp} (bottom figure) as functions of photon energy, where each curve represent an azimuthal angle of incidence from 0 degrees (blue curve) to 90 degrees (red curve), in steps of 5 degrees. The intersections of the Rayleigh lines $(-1,0)_{\mathrm{SiO_2}}$ (dark blue), $(0,-1)_{\mathrm{SiO_2}}$ (green) and $(-1,0)_{\mathrm{air}}$ (brown) with the experimental data, for each energy-angle pair, are overlaid on the data (interpolation is used to draw the lines between any two experimental curves). The LSPRs E_L, E_T and E_Q are indicated in the figure.

ous experimental reports of this resonance for such a truncated low aspect ratio particle in air and supported by a glass substrate. The top right panel shows the E_T resonance excited by s-polarized light along the short axis of the particle at $\phi_0 = 0°$. The field is here more localized inside the particle, causing the significant loss feature as seen in Fig. 5. It is also mainly a dipole response, although of slightly mixed character.

For azimuthal incidence $\phi_0 = 45°$, it is instructive to observe from the bottom left panel of Fig. 7, that for p-polarized light at $\hbar\omega = E_\mathrm{L}$ a strong dipole remains along the long axis of the particle. The latter dipole can be decomposed into a component parallel and perpendicular to the incidence plane, where the perpendicular component then result in polarization conversion from p to s, as observed in e.g. Fig. 6. The situations for s-polarisation at the E_Q and E_T resonances at $\phi_0 = 45°$ are more complicated, but it appears that the field distribution and local field directions at E_Q are considerable more asymmetric than at E_T. We speculate that this may explain the stronger polarization conversion around E_Q than E_T, as seen in the $|r_{ps}| = |r_{sp}|$ amplitude in Fig. 6. An electric field expansion and inspection of only the scattered field may lead to a better understanding of the system, but this is outside the scope of this work.

F. Generalized ellipsometric parameters

It is sometimes favourable to transform the normalized Mueller matrix data into the generalized ellipsometric parameters, such as ψ_{pp} and Δ_{pp}, defined by $r_{\mathrm{pp}}/r_{\mathrm{ss}} = \tan\psi_{\mathrm{pp}}\exp\left(i\Delta_{\mathrm{pp}}\right)$ [23].

The parameter ψ_{pp}, basically conveys similar information to m_{12} in Fig. 3, while Δ_{pp} is a sensitive measure of the relative phase change between p- and s-polarized light at a given azimuthal angle of incidence. This latter information is also included in e.g. the m_{33} and m_{34} elements, but the generalized parameters are somewhat easier to interpret as they do not contain the polarization conversion terms (see Eq. (2)). These parameters are also less noisy in the near infra red part of the spectrum, as they in this work (motivated by the limited depolarization in the $\phi_0 = 0° - 90°$ range) have been calculated from the Mueller Jones matrix fitted to the experimental Mueller matrix [1, 23, 24].

Fig. 8 shows the experimental ψ_{pp} (upper figure) and Δ_{pp} (lower figure) as a function of photon energy, where one curve is presented for each azimuthal angle of incidence ranging from $\phi_0 = 0°$ to $90°$, in steps of $5°$. We clearly observe the dispersive reshaping (as a function of the azimuthal angle of incidence) of the main LSPR resonance E_L as a result of the overlapping of the Rayleigh anomalies with the plasmon resonance. The E_T resonance is similarly shaped by the $(-1,0)_{\mathrm{SiO_2}}$ line, while the E_Q resonance does not seem modified by any Rayleigh anomalies. The offset between the features of the E_L resonance and the $(-1,0)_{\mathrm{SiO_2}}$ line is believed to be due to uncertainty in the lattice parameters (and possibly the dispersion of the substrate and the angle of incidence) when calculating the Rayleigh lines for the experimental data, as the Rayleigh lines were observed to be well localized to these spectral features in the FEM simulations. It is observed that there is no deep dip in the spectrum (as expected from the the first Rayleigh-Wood anomaly), but only a peak/edge. In their multipolar model describing surface lattice resonances (although no substrate nor azimuthal dependency reported), Swiecicki and Sipe discussed the suppression of the Rayliegh-Wood anomaly through interaction of several multipole moments [22]. Furthermore, experimental issues related to reduced coherence can also affect the quality of the resonance and thus suppress the sharp dip. However, the FEM simulations in Fig. 6 provide similar results to the experimental ones.

The Δ_{pp} spectra shows significant relative phase shift between the s and the p component of the reflection amplitudes associated with each resonance. This relative phase shift is observed to span $120°$ upon azimuthal rotation of the sample. The effect of the Rayleigh anomalies are also here observed in the spectra, but not to the same degree as in ψ_{pp}. It is interesting to note that the relative phase is highly sensitive to ϕ_0 in regions where the change in amplitudes is limited, highlighting the general sensitivity of ellipsometric techniques. Furthermore, all Mueller matrix elements which include relative phase changes (in addition to amplitude changes), are expected to supply a high lateral sensitivity to the lateral dimensions of nanostructures [4–11], in addition to the standard reported thickness of layer sensitivity [1]. Hence through fitting a morphological model to the recorded spectrum, a metasurface consisting of identical scatterers may be characterized with high sensitivity to manufacture parameters, an issue that will be discussed further elsewhere.

G. Decomposition and metasurface applications

In terms of metasurface applications, considerable polarization coupling is a major issue and needs to be carefully addressed and included in any design process, such as for combatting e.g. coma and astigmatism in the design of e.g. flat lenses [31]. At normal incidence, each particle is commonly modelled as a retarder. The reflection matrices reported in this work can be tentatively decomposed using the forward decomposition [32, 33]

as the product of a retarder Mueller matrix $\mathbf{M}_R$ and a diattenuator matrix $\mathbf{M}_D$, such that $\mathbf{M} = \mathbf{M}_R \mathbf{M}_D$. The $\mathbf{M}_D$ matrix is then easily calculated from the diattenuation vector $\mathbf{D} = (m_{12}, m_{13}, m_{14})$ thus directly available from the experimental Mueller matrix. It is recalled that the m_{13} element is thus simply the ± 45 degrees diattenuation while the m_{14} is the circular diattenuation. It is striking that we observe here from Fig. 4 a considerable circular diattenuation (± 0.35), which in addition is resonantly enhanced by coupling to Rayleigh anomalies. The circular diattenuation is expected to be accompanied by a circular retardance or optical rotation. The m_{23} and m_{24} elements are consequently complicated functions of both diattenuation and retardance. The linear retardance is associated to the phase-shifts between two linear orthogonal states along the principal axis (i.e. with respect to the orientation of the retardance vector), as often explored in metasurface designs [12, 14]. The forward decomposition of the experimental Mueller matrix results here in a linear retardance spanning 75-177 degrees, while the optical rotation spans as much as ± 45 degrees across the spectral range, where both depends strongly on the azimuthal angle of incidence.

A circular diattenuation of similar amplitude has been reported in arrays of circular holes in a gold film, again supported by a glass substrate [34, 35]. The current system is different as it does not rely on excitation of surface plasmon polaritons, and Brakstad et al. [23] only observed a minor circular diattenuation at oblique incidence for hemispherical particles. On the other hand, strong circular diattenuation has been reported for lattices of e.g. U shaped particles [36]. The complex field patterns in the bottom row of Fig. 7 (at azimuthal incidence $\phi_0 = 45°$), are thus near field patterns corresponding to a far field response revealing linear and circular birefringence and diattenuation. Complete multipolar models [22] or e.g. the reduced Rayleigh equations [11], including the substrate and the azimuthal orientation at oblique incidence, are envisaged to reveal further details of such a complex system.

It is expected that the overlapping of higher order Rayleigh lines with the LSPRs or even e.g. Mie resonances in metasurface designs, will cause a considerable amount of reshaping of the resonances with associated phase shifts. For metasurfaces designed to operate in the visible (many plasmonic designs are today limited to 800-900 nm), it will thus be of high importance to control and design the metasurfaces correctly in order to include the effect of the lattice, both in terms of phase shifts and amplitudes. This will be even further important for metasurfaces operating at higher angles of incidences [37].

5. CONCLUSION

Mueller matrix ellipsometry at oblique incidence reveal a considerable amount of information related to the coupling between the lattice and the plasmon resonances of truncated elliptical gold particles on glass. A direct interpretation of the Mueller matrix can be difficult, but it is shown that through a combination of experimental Mueller matrix data, a Finite Element Model and calculation of Rayleigh lines, it is possible to describe the major spectral features of the optical response of the system. As an example, we presented the power loss and discussed spectral and dispersive features (as a function of azimuthal angle of incidence) for the LSPRs and the Rayleigh lines, therein also for polarization conversion. We identified a quadrupole resonance for elliptical particles supported by a substrate. It is further shown that the interaction of the LSPRs and the lattice through the Rayleigh anomalies (i.e. through

grazing diffracted waves) have a serious impact on the resulting Jones matrix elements, including relative phase changes. Furthermore, circular diattenuation and optical rotation appears important at oblique incidence. It is thus of high importance to understand, measure (monitor and control) and model the interaction between the Rayleigh anomalies and the LSPR for the design and manufacture of metasurfaces.

REFERENCES

1. H. G. Tompkins and E. A. Irene, *Handbook of Ellipsometry* (William Andrew Inc., 2005).
2. H. Fujiwara, ed., *Spectroscopic ellipsometry: principles and applications* (John Wiley & Sons Ltd., 2007).
3. M. Losurdo and K. Hingerl, *Ellipsometry at the nanoscale* (Springer, 2012).
4. S. O'Mullane, N. Keller, and A. C. Diebold, "Modeling ellipsometric measurement of novel 3D structures with RCWA and FEM simulations," Proc. SPIE **9778**, 977805 (2016).
5. D. Dixit, A. Green, E. R. Hosler, V. Kamineni, M. E. Preil, N. Keller, J. Race, J. S. Chun, M. O'Sullivan, P. Khare, W. Montgomery, and A. C. Diebold, "Optical critical dimension metrology for directed self-assembly assisted contact hole shrink," J. Micro/Nanolithography, MEMS, MOEMS **15**, 014004 (2016).
6. D. Dixit, M. Medikonda, A. C. Diebold, B. Peterson, and J. Race, "Mueller matrix optical scatterometry of Si fins patterned using directed self-assembly block copolymer line arrays," in *Proceedings of 25th Annual SEMI Advanced Semiconductor Manufacturing Conference,* (2014), pp. 180–185.
7. B. K. Minhas, S. A. Coulombe, S. Sohail, H. Naqvi, and J. R. McNeil, "Ellipsometric scatterometry for the metrology of sub-0.1-μm-linewidth structures," Appl. Opt. **37**, 5112–5115 (1998).
8. X.-T. Huang and J. Terry, F. L., "Erratum to Spectroscopic ellipsometry and reflectometry from grating (scatterometry) for critical dimension measurement and *in situ*, real-time process monitoring [Thin Solid Films 455-456, 828-836 (2004)]," Thin Solid Films **486**, 339–346 (2004).
9. T. Novikova, A. D. Martino, S. B. Hatit, and B. Drévillon, "Application of mueller polarimetry in conical diffraction for critical dimension measurements in microelectronics," Appl. Opt. **45**, 3688–3697 (2006).
10. M. Foldyna, A. De Martino, E. Garcia-Caurel, R. Ossikovski, C. Licitra, F. Bertin, K. Postava, and Drévillon, "Critical dimension of biperiodic gratings determined by spectral ellipsometry and Mueller matrix polarimetry," Eur. Phys. J. Appl. Phys. **42**, 351–359 (2008).
11. J.-P. Banon, T. Nesse, Z. Ghadyani, M. Kildemo, and I. Simonsen, "Critical dimension metrology of a plasmonic photonic crystal based on mueller matrix ellipsometry and the reduced rayleigh equation," Opt. Lett. **42**, 2631–2634 (2017).
12. N. Yu and F. Capasso, "Flat optics with designer metasurfaces," Nat. Mater. **13**, 139–150 (2014).
13. A. V. Kildishev, A. Boltasseva, and V. M. Shalaev, "Planar photonics with metasurfaces," Science. **339**, 1232009 (2013).
14. F. Ding, A. Pors, and S. I. Bozhevolnyi, "Gradient metasurfaces: a review of fundamentals and applications," Rep. Prog. Phys. **81**, 026401 (2017).
15. I. Staude and J. Schilling, "Metamaterial-inspired silicon nanophotonics," Nat. Photonics **11**, 274–284 (2017).
16. V. Kravets, A. Kabashin, W. Barnes, and A. Grigorenko, "Plasmonic surface lattice resonances: a review of properties and applications," Chem. Rev. **118**, 5912–5951 (2018).
17. D. Khlopin, F. Laux, W. P. Wardley, J. Martin, G. A. Wurtz, J. Plain, N. Bonod, A. V. Zayats, W. Dickson, and D. Gérard, "Lattice modes and

plasmonic linewidth engineering in gold and aluminum nanoparticle arrays," J. Opt. Soc. Am. B **34**, 691–700 (2017).

18. S. R. K. Rodriguez, A. Abass, B. Maes, O. T. A. Janssen, G. Vecchi, and J. Gómez Rivas, "Coupling bright and dark plasmonic lattice resonances," Phys. Rev. X **1**, 021019 (2011).

19. P. Offermans, M. C. Schaafsma, S. R. K. Rodriguez, Y. Zhang, M. Crego-Calama, S. H. Brongersma, and J. Gómez Rivas, "Universal scaling of the figure of merit of plasmonic sensors," ACS Nano **5**, 5151–5157 (2011).

20. Y. Francescato, V. Giannini, and S. A. Maier, "Plasmonic systems unveiled by Fano resonances," ACS Nano **6**, 1830–1838 (2012).

21. G. Vecchi, V. Giannini, and J. Gómez Rivas, "Surface modes in plasmonic crystals induced by diffractive coupling of nanoantennas," Phys. Rev. B **80**, 201401 (2009).

22. S. D. Swiecicki and J. E. Sipe, "Surface-lattice resonances in two-dimensional arrays of spheres: Multipolar interactions and a mode analysis," Phys. Rev. B **95**, 195406 (2017).

23. T. Brakstad, M. Kildemo, Z. Ghadyani, and I. Simonsen, "Dispersion of polarization coupling, localized and collective plasmon modes in a metallic photonic crystal mapped by Mueller matrix ellipsometry," Opt. Express **23**, 22800–22815 (2015).

24. M. Kildemo, J.-P. Banon, A. Baron, B. B. Svendsen, T. Brakstad, and I. Simonsen, "Optical response of gold hemispheroidal lattices on transparent substrates," Appl. Surf. Sci. **421**, 593–600 (2017).

25. R. M. A. Azzam and N. M. Bashara, *Ellipsometry and Polarized Light* (North-Holland Publishing Company, 1977).

26. P. S. Hauge, R. H. Muller, and C. G. Smith, "Conventions and formulas for using the mueller-stokes calculus in ellipsometry," Surf. Sci. **96**, 81 – 107 (1980).

27. P. A. Letnes, A. A. Maradudin, T. Nordam, and I. Simonsen, "Calculation of all elements of the Mueller matrix for scattering of light from a two-dimensional randomly rough metal surface," Phys. Rev. A **86**, 031803(R) (2012).

28. R. Ossikovski and K. Hingerl, "General formalism for partial spatial coherence in reflection Mueller matrix polarimetry," Opt. Lett. **41**, 4044–4047 (2016).

29. O. Arteaga, "Useful Mueller matrix symmetries for ellipsometry," Thin Solid Films **571**, 584–588 (2014).

30. B. N. Khlebtsov and N. G. Khlebtsov, "Multipole plasmons in metal nanorods: scaling properties and dependence on particle size, shape, orientation, and dielectric environment," J. Phys. Chem. C **111**, 11516–11527 (2007).

31. F. Aieta, P. Genevet, M. Kats, and F. Capasso, "Aberrations of flat lenses and aplanatic metasurfaces," Opt. Express **21**, 31530–31539 (2013).

32. S.-Y. Lu and R. A. Chipman, "Interpretation of Mueller matrices based on polar decomposition," J. Opt. Soc. Am. A **13**, 1106–1113 (1996).

33. R. Ossikovski, A. D. Martino, and S. Guyot, "Forward and reverse product decompositions of depolarizing mueller matrices," Opt. Lett. **32**, 689–691 (2007).

34. O. Arteaga, B. M. Maoz, S. Nichols, G. Markovich, and B. Kahr, "Complete polarimetry on the asymmetric transmission through subwavelength hole arrays," Opt. Express **22**, 13719–13732 (2014).

35. B. Gompf, J. Braun, T. Weiss, H. Giessen, M. Dressel, and U. Hübner, "Periodic nanostructures: Spatial dispersion mimics chirality," Phys. Rev. Lett. **106**, 185501 (2011).

36. N. Guth, B. Gallas, J. Rivory, J. Grand, A. Ourir, G. Guida, R. Abdeddaim, C. Jouvaud, and J. de Rosny, "Optical properties of metamaterials: Influence of electric multipoles, magnetoelectric coupling, and spatial dispersion," Phys. Rev. B **85**, 115138 (2012).

37. S. M. Kamali, E. Arbabi, A. Arbabi, Y. Horie, M. Faraji-Dana, and A. Faraon, "Angle-multiplexed metasurfaces: Encoding independent wavefronts in a single metasurface under different illumination angles," Phys. Rev. X **7**, 041056 (2017).